A snapshot of the earliest stages of normal fault development

Ahmed Alghuraybi[1], Rebecca E. Bell[1], and Christopher A-L. Jackson[2]

[1]Basins Research Group (BRG), Earth Science and Engineering, Imperial College, Prince Consort Road, London, SW7 2BP, UK

[2]Department of Earth, Atmospheric and Environmental Sciences, The University of Manchester, Williamson Building, Oxford Road, Manchester, M13 9PL, UK

ABSTRACT

Despite decades of study, models for the growth of normal faults lack a temporal framework within which to understand how these structures accumulate displacement and lengthen through time. Here, we use borehole and high-quality 3D seismic reflection data from offshore Norway to quantify the lateral (0.2-1.8 $mmyr^{-1}$) and vertical (0.004-0.02 $mmyr^{-1}$) propagation rates (averaged over 12-44 Myr) for several long (up to 43 km), moderate displacement (up to 225 m) layer-bound faults that we argue provide a unique, essentially 'fossilised' snapshot of the earliest stage of fault growth. We show that lateral propagation rates are 90 times faster than displacement rates during the initial 25% of their lifespan suggesting that these faults lengthened much more rapidly than they accrued displacement. Although these faults have slow displacement rates compared with data compiled from 30 previous studies, they have comparable lateral propagation rates. This suggests that the unusual lateral propagation to displacement rate ratio is likely due to fault maturity, which highlights a need to document both

displacement *and* lateral propagation rates to further our understanding of how faults evolve across various temporal and spatial scales.

INTRODUCTION

There are currently two end-member fault growth models: (i) the 'propagating fault model' and (ii) the 'constant length model'. The former arises from the apparent scaling relationship between maximum fault displacement (D_{max}) and length (L_{max}) and proposes that faults grow by simultaneously accumulating length and displacement (where D_{max}/L_{max} typically ranges between 1 – 0.01; e.g., Watterson, 1986; Walsh and Watterson, 1988; Cowie and Scholz, 1992; Schlische et al., 1996; Walsh et al., 2003). However, global D_{max}-L_{max} datasets show a high degree of scatter (e.g., Rotevatn et al., 2019), which may reflect, for example, differences in the geological setting within which the studied fault network formed, or uncertainties in measuring the key geometric parameters due to seismic imaging quality or outcrop extent (e.g., Walsh and Watterson, 1988; Gillespie et al., 1992; Kim and Sanderson, 2005). An alternative interpretation is that this variability results from fault maturity, related to the fact that some faults may attain their near-final lengths before accumulating significant displacement (i.e., the constant-length fault model; e.g., Walsh et al., 2002; Meyer et al., 2002; Nicol et al., 2005; Nicol et al., 2016; Childs et al., 2017; Rotevatn et al., 2019). Regardless of the precise mode of growth, previous studies have shown that strong mechanical anisotropy in the faulted, horizontally layered host rock can restrict the vertical propagation of faults (e.g., Nicol et al., 1996; Soliva et al., 2005; Roche et al., 2013). Faults forming in these rocks may have anomalously high fault aspect ratios (i.e., 3 – 13, compared to 1 – 3 for more typical faults) and strikingly low D-L scaling relationships (i.e., $D_{max}/L < 0.01$) (e.g., Nicol et al., 1996; Schlische et al., 1996; Soliva et al., 2005; Roche et al., 2013).

The rate at which faults lengthen and accumulate displacement is a key element of their kinematic history and influences the role they play in controlling the geomorphology, seismic hazard, and resource potential of rift basins (e.g., Walsh et al., 2003). Depending on the period and type of observation, displacement rates vary. For example, over relatively short observational periods (10s years), GPS/geodetic data show that displacement rates can be relatively fast (>10 mm yr^{-1}) and highly variable (e.g., Briole et al., 2000; Wallace et al., 2014) compared to longer-period, typically more stable geological slip rates (<1 mm yr^{-1}) derived from seismic reflection or field data (e.g., Cowie et al., 2012; Mouslopoulou et al., 2012). In contrast, lateral propagation rates are less frequently reported in fault growth studies especially over short observational periods. Our current understanding of fault growth, in particular how changes in fault geometry relate to fluctuations in displacement rate, remains uncertain. For example, fault growth models need to quantify both lateral and displacement rates to provide a temporal framework of fault growth (e.g., Walsh et al., 2002; Rotevatn et al., 2019), given this may reconcile the differences between short-term geodetic rates and long-term geological rates. Constraining the patterns and rates of fault growth requires the analysis of syn-kinematic strata (i.e., strata deposited whilst the fault is active), although this is commonly poorly imaged in seismic reflection data or not preserved in the field (e.g., Rotevatn et al., 2019).

We here use age-constrained, high-quality 3D seismic reflection and borehole data to determine the lateral and vertical propagation rates for several layer-bound faults that: (i) exhibit unusually high (up to 25) aspect ratios; (ii) have anonymously low (c. 0.001) D_{max}-L_{max} scaling relationships; and (iii) were associated with continuous, strike-elongate depocenters during the very earliest stages of their development, all features consistent with the constant-length model. We propose that these faults provide a unique snapshot of the earliest stage of fault growth.

GEOLOGICAL SETTING

The study area is in the SW Barents Sea (Fig. 1A), offshore northern Norway where multiple phases of rifting, including one in the Middle Jurassic to Early Cretaceous that formed the faults studied here, shaped the large-scale structure of the region (e.g., Faleide et al., 2008). The tectonic (i.e., non-gravitational) origin of the studied fault system is supported by the fact that they: (i) strike perpendicular to the NNW-SSE extension direction associated with Middle Jurassic to Early Cretaceous rifting; and (ii) the basal detachment is not tilted in the direction of fault dip. The faults developed in Triassic to Lower Cretaceous clastic rocks deposited on Caledonian crystalline basement (e.g., Doré, 1995). The faulted host rock is characterized by strong mechanical competency contrast between alternating intervals of relatively weak, mudstone-rich strata (i.e., Upper Permian) and mechanically stronger, siltstone- and sandstone-rich layers (i.e., Triassic) (Fig. 1B).

DATA AND METHODS

Geometric analysis

We use pre-stack time-migrated 3D seismic reflection data covering c. 533 km^2 and with an estimated vertical resolution = 12.5 – 25 m in the depth range of interest (see Appendix 1). These data allow us to map and describe the plan-view and cross-sectional geometry of the studied fault network, and by collecting throw data for nine horizons (six age-constrained by well data and three of unknown age that mark distinct changes in seismic facies) to show how throw varies across the fault surfaces (Fig. 1B). The horizons' ages were constrained by wellbore 7124/4-1S. We also produce isochron (time-thickness) maps, throw strike-projections, and expansion index (EI) analysis to further describe the geometry of the fault network and critically assess associated variations in the thickness of syn-kinematic strata (see review by Walsh and Watterson, 1991 and Jackson et al., 2017).

Kinematic analysis

We estimate the lateral fault tip propagation rate by taking the fault half-length as measured at the base of the syn-kinematic interval and dividing it by the time interval to the next age-constrained horizon that shows across-fault thickening (i.e., we establish the duration and length of major depocenter development and calculate the bi-directional propagation rate of the fault tips; cf. Childs et al., 2003). Similarly, we calculate the displacement rate by dividing the maximum displacement by the time interval to the next age-constrained horizon (e.g., Nicol et al., 1997; Bell et al., 2009). We provide detailed descriptions of our methods in Appendix 2.

RESULTS

Fault network geometry

The studied fault network consists of 15 Late Jurassic faults offsetting Early Triassic to Early Cretaceous stratigraphy (Fig. 1B, C). Most of these faults tip-out downwards in mudstone-dominated, Permian strata, die-out upwards into Late Jurassic – Early Cretaceous strata, and are associated with Upper Jurassic growth strata (i.e., they were active in the Late Jurassic; Fig. 1B).

These faults are not associated with clear fault bends, abandoned splays or relays (Fig. 1C). The majority of these faults are unusual in that they are: i) notably under-displaced with respect to their lengths (D_{max}/L_{max} = c. 0.001; Fig. 1A); and ii) have anomalously high aspect ratios (>13; Fig. 1D). Here, we present a detailed geometric analysis of two faults from the fault network; not only do these have the highest aspect ratios, but they are also particularly large and thus well-imaged.

Fault 8 (F8) – Observations

F8 is the longest fault in the network (c. 43 km; Fig. 1C). It has a maximum throw of c. 72 ms (c. 110 m; see velocity models in Appendix 3) and a maximum total displacement of c. 130 m (Fig. 2A). F8 strikes E-W, dips to the N, and has the highest aspect ratio of any fault in the network (c. 24.6; Fig. 1). F8 appears to have multiple along-strike throw maxima, all of which are located at the base of the syn-kinematic interval (i.e., base Upper Jurassic; Fig. 2A). Upper Jurassic strata thicken across the fault (EI up to 2.2), with a key observation being that the lowermost reflections in this package onlap onto the base syn-kinematic horizon immediately adjacent to the fault tips (H4) (Fig. 2).

Fault 11 (F11) – Observations

F11 is an E-W striking, N-dipping fault that is c. 31 km long (Fig. 1C). It has a maximum throw of c. 55 ms (c. 70 m) and a maximum total displacement of c. 104 m (Fig. 2A). F11 has an aspect ratio of c. 19 with Upper Jurassic strata thickening across the fault (EI values up to 1.7; Fig. 2A, B). Similar to F8, F11 appears to bound a single, strike-elongate, Upper Jurassic depocenter (Fig. 2B). However, F11 exhibits a broad, bell-shaped throw-length profile at the base syn-kinematic level (H4), with its throw maximum skewed towards the west (Figs. 2A). A key observation is that Upper Jurassic growth strata clearly thicken across the fault just inboard of its tips (Fig. 2B, C).

Interpretation

Growth strata show that F8 and F11 were active from 201.3 – 157.3 Ma (i.e., in the Late – Early Jurassic; Fig. 2B), with the presence of multiple throw maxima on some of these faults (F8; Fig. 2A) providing geometric evidence that they grew by segment linkage (e.g., Cartwright et al., 1995). However, the lack of obvious bends, breached relays, or abandoned splays suggests that the precursor segments did not overlap, and may have formed part of a single, kinematically linked structure from their inception (e.g., Childs et al., 2017). This is supported by the fact that the thickening we observe here is seen along-strike of the faults and is associated with onlap of the lowermost syn-kinematic strata onto pre-kinematic immediately inboard of the lateral fault tips (Fig. 2B, C).

GROWTH RATES OF FAULTS

The studied faults have relatively slow slip rates (0.0009 – 0.004 mm/yr^{-1}) when averaged over the 44 Myr period of fault activity. However, by assuming a constant sedimentation rate, we can estimate the age of the earliest stage of fault activity, or the age at which the near-final fault length was established, that is associated with the development of the strike-elongate depocenters (Fig. 2B). By using this estimated age (12 Myr), we infer displacement rates of (0.004 – 0.02 mm yr^{-1}) for the earliest detectable stage of fault activity. We then compare these slip rates with data from 29 other datasets (see Appendix 4 for a full list of references), showing the studied fault network having relatively low slip rates even when averaged over the estimated 12 Myr period (Fig. 3A). Even though our slip rates are relatively low, they are similar to rates measured over similar time scales (i.e., >10^7 years; Fig. 3A) in the North Sea (Nicol et al., 1997; Bell et al., 2014), the Timor Sea (Meyer et al., 2002), the Basin & Range and Taranaki Rift (Mouslopoulou et al., 2009), or for faults with similar trace lengths (>10^4 km; Fig. 3B; Lathrop et al., 2021).

Despite having low displacement rates, the studied fault network is associated with high lateral propagation rates (0.2 – 1.8 mm/year) that are 1-2 orders-of-magnitude higher than other faults active over similar durations (i.e., >10^6 years; Fig. 3A) (Bell et al., 2014; Lathrop et al., 2021). By taking the ratio between lateral and vertical propagation rates (i.e., to quantify the difference between lateral and vertical deformation), we observe that independent of fault length (and accuracy of our age estimate of 12 Myr), the studied faults propagated laterally much more rapidly (i.e., 90 times faster) than they accumulated displacement (see Appendix 5), a value 2-3 orders of magnitude higher than other seismically imaged faults of similar length (e.g., Bell et al., 2009; Lathrop et al., 2021). This observation suggests that the studied network captures faults during their very earliest stage of development, when they were growing in accordance with the constant-length model. They had rapidly lengthened and reached their near-final lengths but did not have a chance to accumulate significant additional displacement before becoming inactive (e.g., Walsh et al., 2002; Meyer et al., 2002; Nicol et al., 2005; Nicol et al., 2016; Childs et al., 2017). Why the faults became inactive is unknown, although we suspect this is related to strain localization on to the nearby, very large (c. 2 km displacement), basement-rooted, Troms-Finnmark Fault Complex (TFFC), which continued to be active until the Eocene (e.g., Alghuraybi et al., 2021). This effect of strain localization is amplified by virtue of having a weak mudstone layer at the bottom of the faulted interval, which inhibited downward propagation of these faults and limited the accumulation of additional displacement. As a result, these faults have large aspect ratios and were characterized by lateral propagation rates that were significantly faster than displacement rate.

The highest aspect ratio ever reported for a natural normal fault is 12 (Nicol et al., 1996; Soliva et al., 2005; Roche et al., 2013); this is significantly lower than the highest aspect ratio we observe here (c. 25). In fact, five of the studied faults have aspect ratios >>13 (Fig. 1D). Numerical models, motivated by observations from meter-scale fault networks in layered carbonate rocks, show that aspect ratios can vary through time, increasing when the faults interact with layers that restrict their onwards vertical propagation, before decreasing again when they are able to breach those layers (e.g., Soliva et al., 2005; Roche et al., 2013). Our study suggests that this process may occur at substantially larger scales than previous reported, meaning aspect ratio variability is a fundamental aspect of fault growth across scales in mechanically layered rocks.

Our slip rate data compilation builds on previous works (e.g., Nicol et al., 2005; Mouslopoulou et al., 2009; Nicol et al., 2020) and includes lateral propagation and displacement rate data measured over a range of temporal scales using different methods (geodetic, GPS, field observations, seismic refraction, and reflection data). Our updated database shows a high degree of scatter for slip rates over timescales $>10^5$ years, which could simply reflect the fact that more data has been collected over these longer timescales. It is also clear from our dataset that lateral propagation rates are often not reported or less frequently documented compared to displacement rates. Based on this we argue there is a need to collect more data measured over shorter temporal scales (i.e., especially 10^2 – 10^5 years) and to document, where possible, both displacement *and* lateral propagation rates. By doing so, we can further our understanding of how faults evolve across various temporal and spatial scales.

ACKNOWLEDGEMENT

The results presented here are part of AA's PhD research at Imperial College London, funded by Saudi Aramco. We thank the Norwegian Petroleum Directorate the publicly data (https://portal.diskos.cgg.com/whereoil-data/) and Schlumberger for Petrel software.

FIGURE CAPTIONS

Figure 1: (A) Map showing study area location and displacement – length data from the studied fault network plotted on a global displacement-length plot modified from Rotevatn et al. (2019). (B) A representative seismic cross-section highlighting the geometry of the studied faults and horizon's age and lithology as constrained by wellbore 7124/4-1S. (C) A time-structure map of the base syn-kinematic unit (H4) with a white-dashed line indicating the location of the seismic section in (B). (D) Aspect ratio (length/height) distribution of the studied fault network with dashed-horizontal lines showing average aspect ratios of "blind isolated normal faults in layered sequences" (yellow), maximum aspect ratio of restricted faults (red) (Nicol et al., 1996) and maximum aspect ratio for faults cutting formations with strong mechanical contrast (green) (Roche et al., 2013).

Figure 2: (A) Strike-projected throw distributions and Expansion Index values along Faults 8 and 11. (B) Isochron (time-thickness) maps for syn-kinematic unit (1) and lowermost package of that unit (2) showing across-fault thickening in the smallest resolvable interval. (C) un-

interpreted and interpreted seismic sections along-strike of Fault 8 with a red arrow highlighting the observed onlap relationship.

Figure 3: (A) slip rate data across various timescales for the studied fault network (cross) and literature data (circle). Vertical slip rate is shown in blue while lateral propagation rate is shown in green. Error-bars account for uncertainty in age-constrain (10-44 Myr). Another version of this plot is provided in Appendix 4 where each literature study is clearly indicated, and the literature data is provided in Appendix 6. (B) slip rate data across various fault lengths.

REFERENCES

Alghuraybi, A., Bell, R. E., & Jackson, C. A.-L., 2021, The geometric and temporal evolution of fault-related folds constrain normal fault growth patterns, Barents Sea, offshore Norway: Basin Research, v.00, p. 1– 22, https://doi.org/10.1111/bre.12633

Bell, R. E., Jackson, C. A. L., Whipp, P. S., & Clements, B., 2014, Strain migration during multiphase extension: Observations from the northern North Sea: Tectonics, v. 33, p. 1936–1963, https://doi.org/10.1002/2014TC003551

Bell, R. E., McNeill, L. C., Bull, J. M., Henstock, T. J., Collier, R. L., & Leeder, M. R., 2009, Fault architecture, basin structure and evolution of the Gulf of Corinth Rift, central Greece: Basin Research, v. 21, p. 824-855.

Briole, P., Rigo, A., Lyon-Caen, H., Ruegg, J. C., Papazissi, K., Mitsakaki, C., ... & Deschamps, A., 2000, Active deformation of the Corinth rift, Greece: results from repeated Global Positioning System surveys between 1990 and 1995: Journal of Geophysical Research: Solid Earth, v. 105, p. 25605-25625.

Cartwright, J. A., Trudgill, B. D., & Mansfield, C. S., 1995, Fault growth by segment linkage: an explanation for scatter in maximum displacement and trace length data from the Canyonlands Grabens of SE Utah: Journal of Structural Geology, v. 17, p. 1319–1326, https://doi.org/10.1016/0191-8141(95)00033-A

Childs, C., Nicol, A., Walsh, J. J., & Watterson, J., 2003, The growth and propagation of synsedimentary faults: Journal of Structural geology, v. 25, p. 633-648.

Childs, Conrad, Holdsworth, R. E., Jackson, C. A. L., Manzocchi, T., Walsh, J. J., & Yielding, G., 2017, Introduction to the geometry and growth of normal faults: Geological Society Special Publication, v. 439, p. 1–9, https://doi.org/10.1144/SP439.24

Cowie, P. A., & Scholz, C. H., 1992, Displacement-length scaling relationship for faults: data synthesis and discussion: Journal of Structural Geology, v. 14, p. 1149-1156.

Cowie, P. A., Roberts, G. P., Bull, J. M., & Visini, F., 2012, Relationships between fault geometry, slip rate variability and earthquake recurrence in extensional settings: Geophysical Journal International, v. 189, p. 143-160.

Doré, A. G., 1995, Barents Sea Geology, Petroleum Resources and Commercial Potential: Arctic, v. 48, p. 207–221, http://www.jstor.org/stable/40511656

Faleide, J. I., Tsikalas, F., Breivik, A. J., Mjelde, R., Ritzmann, O., Engen, Ø., Wilson, J., & Eldholm, O., 2008, Structure and evolution of the continental margin off Norway and the Barents Sea: Episodes, v. 31, p. 82–91, https://doi.org/10.18814/epiiugs/2008/v31i1/012

Gillespie, P. A., Walsh, J. T., & Watterson, J., 1992, Limitations of dimension and displacement data from single faults and the consequences for data analysis and interpretation: Journal of Structural Geology, v. 14, p. 1157-1172.

Jackson, Christopher A.L., Bell, R. E., Rotevatn, A., & Tvedt, A. B. M., 2017, Techniques to determine the kinematics of synsedimentary normal faults and implications for fault growth models: Geological Society Special Publication, v. 439, p. 187–217, https://doi.org/10.1144/SP439.22

Kim, Y. S., & Sanderson, D. J., 2005, The relationship between displacement and length of faults: a review: Earth-Science Reviews, v. 68, p. 317-334.

Lathrop, B. A., Jackson, C. A.-L., Bell, R. E., & Rotevatn, A., 2021, Normal fault kinematics and the role of lateral tip retreat: An example from offshore NW Australia: Tectonics, v. 40, e2020TC006631, https://doi. org/10.1029/2020TC006631

Meyer, V., Nicol, A., Childs, C., Walsh, J. J., & Watterson, J., 2002, Progressive localisation of strain during the evolution of a normal fault population: Journal of Structural Geology, v. 24, p. 1215-1231, https://doi.org/10.1016/S0191-8141(01)00104-3.

Mouslopoulou, V., Walsh, J. J., & Nicol, A., 2009, Fault displacement rates on a range of timescales: Earth and Planetary Science Letters, v. 278, p. 186-197, https://doi.org/10.1016/j.epsl.2008.11.031

Mouslopoulou, V., Nicol, A., Walsh, J. J., Begg, J. G., Townsend, D. B., & Hristopulos, D. T., 2012, Fault-slip accumulation in an active rift over thousands to millions of years and the importance of paleoearthquake sampling: Journal of Structural Geology, v. 36, p. 71-80, https://doi.org/10.1016/j.jsg.2011.11.010

Nicol, A., Watterson, J., Walsh, J. J., & Childs, C., 1996, The shapes, major axis orientations and displacement patterns of fault surfaces: Journal of Structural Geology, v. 18, p. 235-248, https://doi.org/10.1016/S0191-8141(96)80047-2

Nicol, A., Walsh, J. J., Watterson, J., & Underhill, J. R., 1997, Displacement rates of normal faults: Nature, v. 390, p. 157-159, https://doi.org/10.1038/36548

Nicol, A., Walsh, J. J., Manzocchi, T., & Morewood, N., 2005, Displacement rates and average earthquake recurrence intervals on normal faults: Journal of Structural Geology, v. 27, p. 541-551, https://doi.org/10.1016/j.jsg.2004.10.009

Nicol, A., Robinson, R., Van Dissen, R. J., & Harvison, A., 2016, Variability of recurrence interval and single-event slip for surface-rupturing earthquakes in New Zealand: New Zealand Journal of Geology and Geophysics, v. 59, p. 97-116, https://doi.org/10.1080/00288306.2015.1127822

Nicol, A., Mouslopoulou, V., Begg, J., & Oncken, O., 2020, Displacement accumulation and sampling of paleoearthquakes on active normal faults of Crete in the eastern Mediterranean: Geochemistry, Geophysics, Geosystems, v. 21, e2020GC009265, https://doi. org/10.1029/2020GC009265

Roche, V., Homberg, C., & Rocher, M., 2013, Fault nucleation, restriction, and aspect ratio in layered sections: Quantification of the strength and stiffness roles using numerical modeling: Journal of Geophysical Research: Solid Earth, v. 118, p. 4446-4460, doi:10.1002/jgrb.50279

Rotevatn, A., Jackson, C. A. L., Tvedt, A. B., Bell, R. E., & Blækkan, I., 2019, How do normal faults grow?: Journal of Structural Geology, v. 125, p. 174-184, https://doi.org/10.1016/j.jsg.2018.08.005

Schlische, R. W., Young, S. S., Ackermann, R. V., & Gupta, A., 1996, Geometry and scaling relations of a population of very small rift-related normal faults: Geology, v. 24, p. 683-686, https://doi.org/10.1130/0091-7613(1996)024<0683:GASROA>2.3.CO;2

Soliva, R., & Benedicto, A., 2005, Geometry, scaling relations and spacing of vertically restricted normal faults: Journal of Structural Geology, v. 27, p. 317-325, https://doi.org/10.1016/j.jsg.2004.08.010

Wallace, L. M., Ellis, S., Little, T., Tregoning, P., Palmer, N., Rosa, R., ... & Kwazi, J., 2014, Continental breakup and UHP rock exhumation in action: GPS results from the Woodlark Rift, Papua New Guinea: Geochemistry, Geophysics, Geosystems, v. 15, p. 4267-4290, https://doi.org/10.1002/2014GC005458

Walsh, J. J., & Watterson, J., 1988, Analysis of the relationship between displacements and dimensions of faults: Journal of Structural geology, v. 10, p. 239-247, https://doi.org/10.1016/0191-8141(88)90057-0

Walsh, J. J., & Watterson, J., 1991, Geometric and kinematic coherence and scale effects of normal fault systems. *in* Roberts, A. M., Yielding, G., Freemen, B., eds., The Geometry of Normal Faults: Geological Society, London, Special Publication, 186, p. 157-170, https://doi.org/10.1144/GSL.SP.1991.056.01.13

Walsh, J. J., Bailey, W. R., Childs, C., Nicol, A., & Bonson, C. G., 2003, Formation of segmented normal faults: A 3-D perspective: Journal of Structural Geology, v. 25, p. 1251–1262, https://doi.org/10.1016/S0191-8141(02)00161-X

Walsh, J. J., Nicol, A., & Childs, C., 2002, An alternative model for the growth of faults: Journal of Structural Geology, v. 24, p. 1669–1675, https://doi.org/10.1016/S0191-8141(01)00165-1

Watterson, J., 1986, Fault dimensions, displacements and growth: Pure and Applied Geophysics, v. 124, p. 365-373, https://doi.org/10.1007/BF00875732

Figure 1

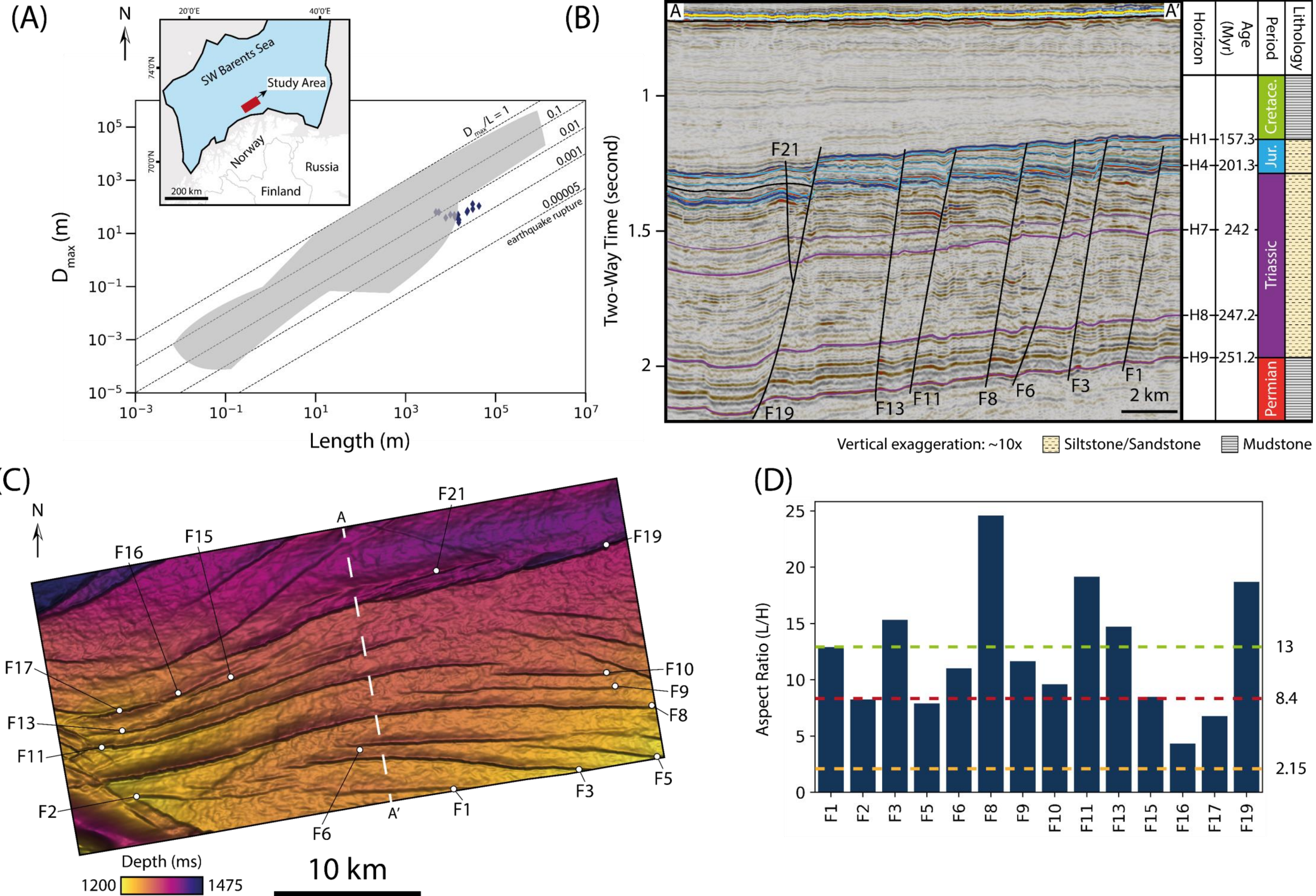
(A)
N
20°0'E
40°0'E
74°0'N
70°0'N
SW Barents Sea
Study Area
Norway
Russia
Finland
200 km
$D_{max}/L = 1$
0.1
0.01
0.001
0.00005
earthquake rupture
D_{max} (m)
Length (m)
(B)
A
A'
F21
F19
F13
F11
F8
F6
F3
F1
2 km
Two-Way Time (second)
Horizon
Age (Myr)
Period
Lithology
H1 157.3
H4 201.3
H7 242
H8 247.2
H9 251.2
Cretace.
Jur.
Triassic
Permian
Vertical exaggeration: ~10x
Siltstone/Sandstone
Mudstone
(C)
N
A
A'
F21
F19
F16
F15
F17
F13
F11
F2
F6
F1
F3
F5
F10
F9
F8
Depth (ms)
1200
1475
10 km
(D)
Aspect Ratio (L/H)
13
8.4
2.15
F1
F2
F3
F5
F6
F8
F9
F10
F11
F13
F15
F16
F17
F19

Figure 2

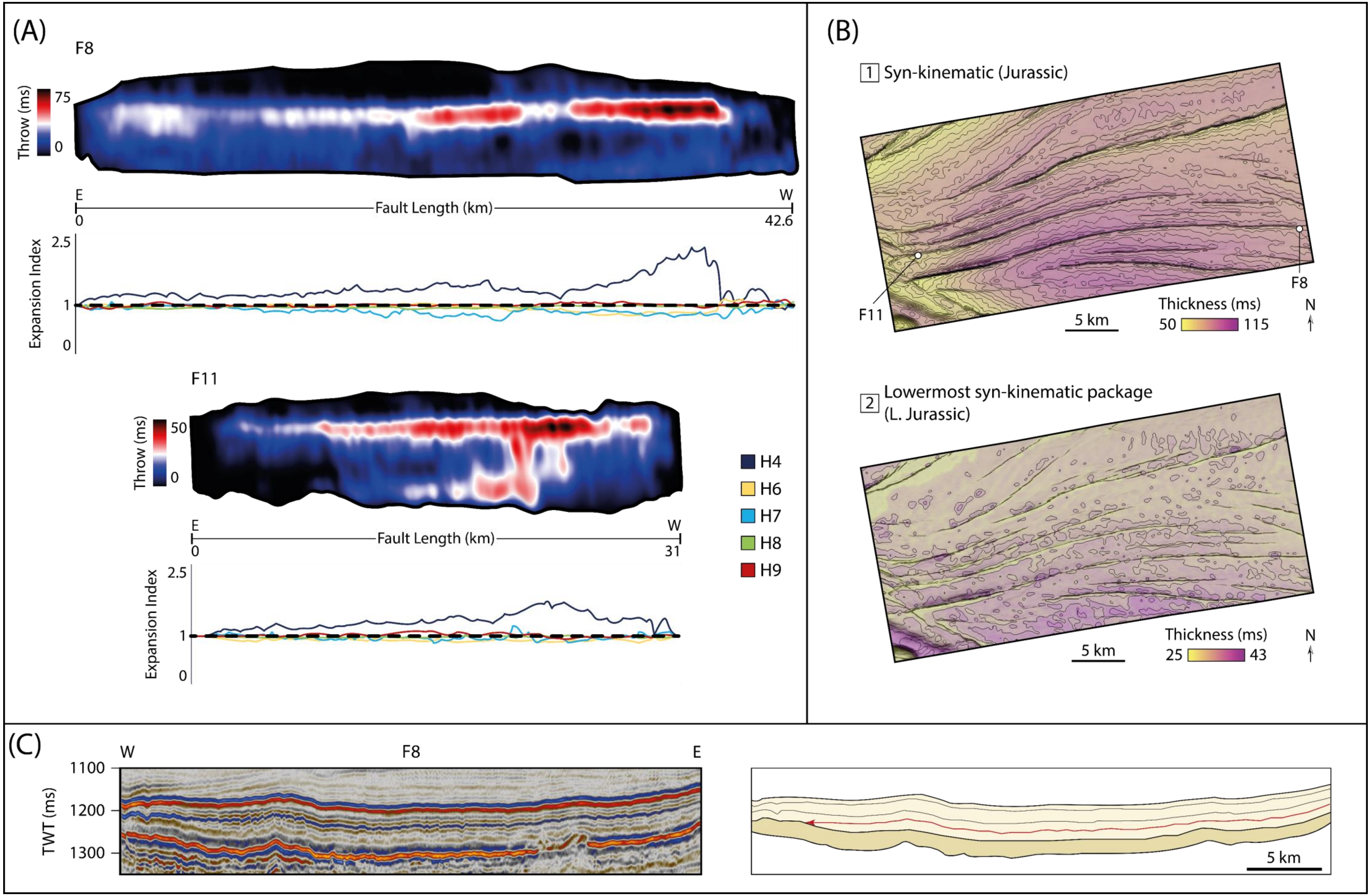

(A)
F8
Throw (ms)
75
0
E
W
Fault Length (km)
0
42.6
Expansion Index
2.5
1
0
F11
Throw (ms)
50
0
E
W
Fault Length (km)
0
31
Expansion Index
2.5
1
0
H4
H6
H7
H8
H9
(B)
1 Syn-kinematic (Jurassic)
F11
F8
5 km
Thickness (ms)
50
115
N
2 Lowermost syn-kinematic package
(L. Jurassic)
5 km
Thickness (ms)
25
43
N
(C)
W
F8
E
TWT (ms)
1100
1200
1300
5 km

Figure 3

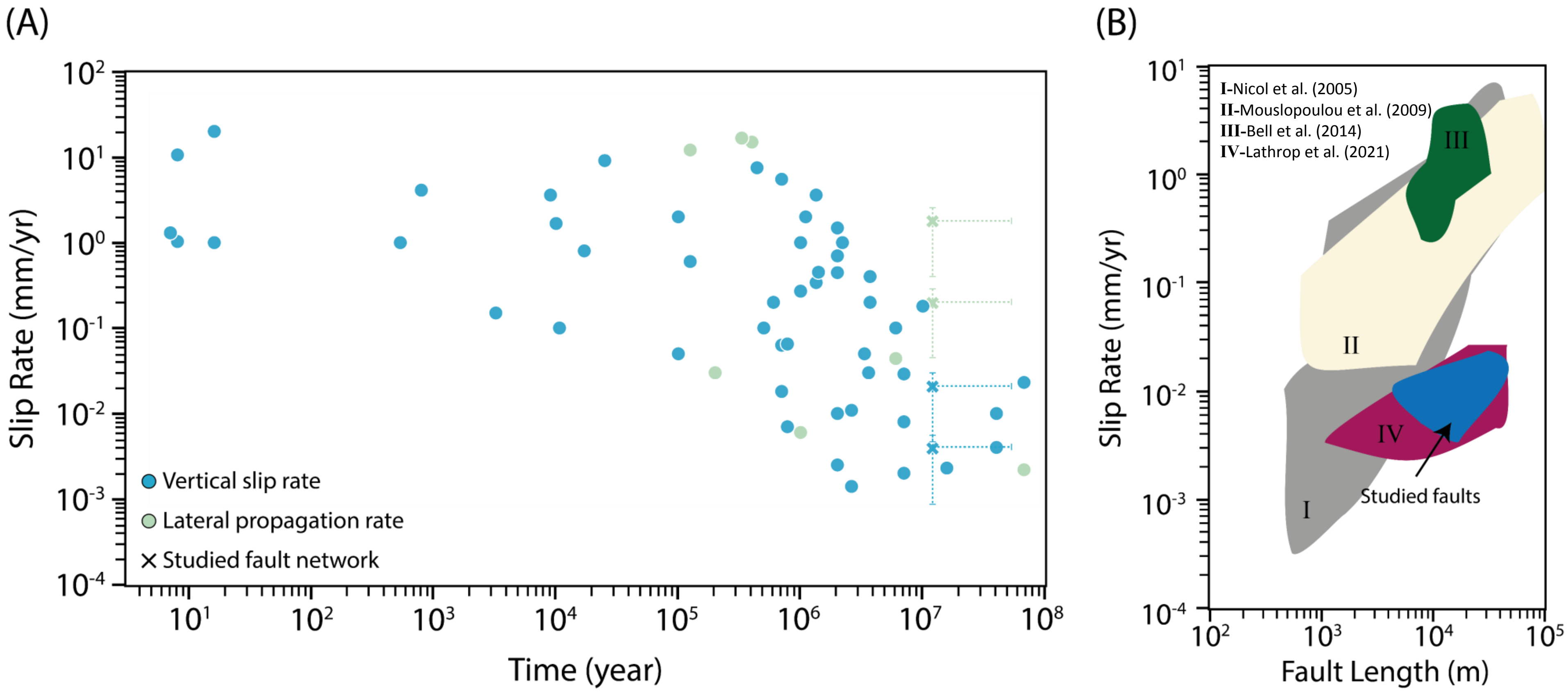

(A)
Slip Rate (mm/yr)
Time (year)
Vertical slip rate
Lateral propagation rate
Studied fault network
(B)
I-Nicol et al. (2005)
II-Mouslopoulou et al. (2009)
III-Bell et al. (2014)
IV-Lathrop et al. (2021)
Studied faults
Slip Rate (mm/yr)
Fault Length (m)

Appendix 1

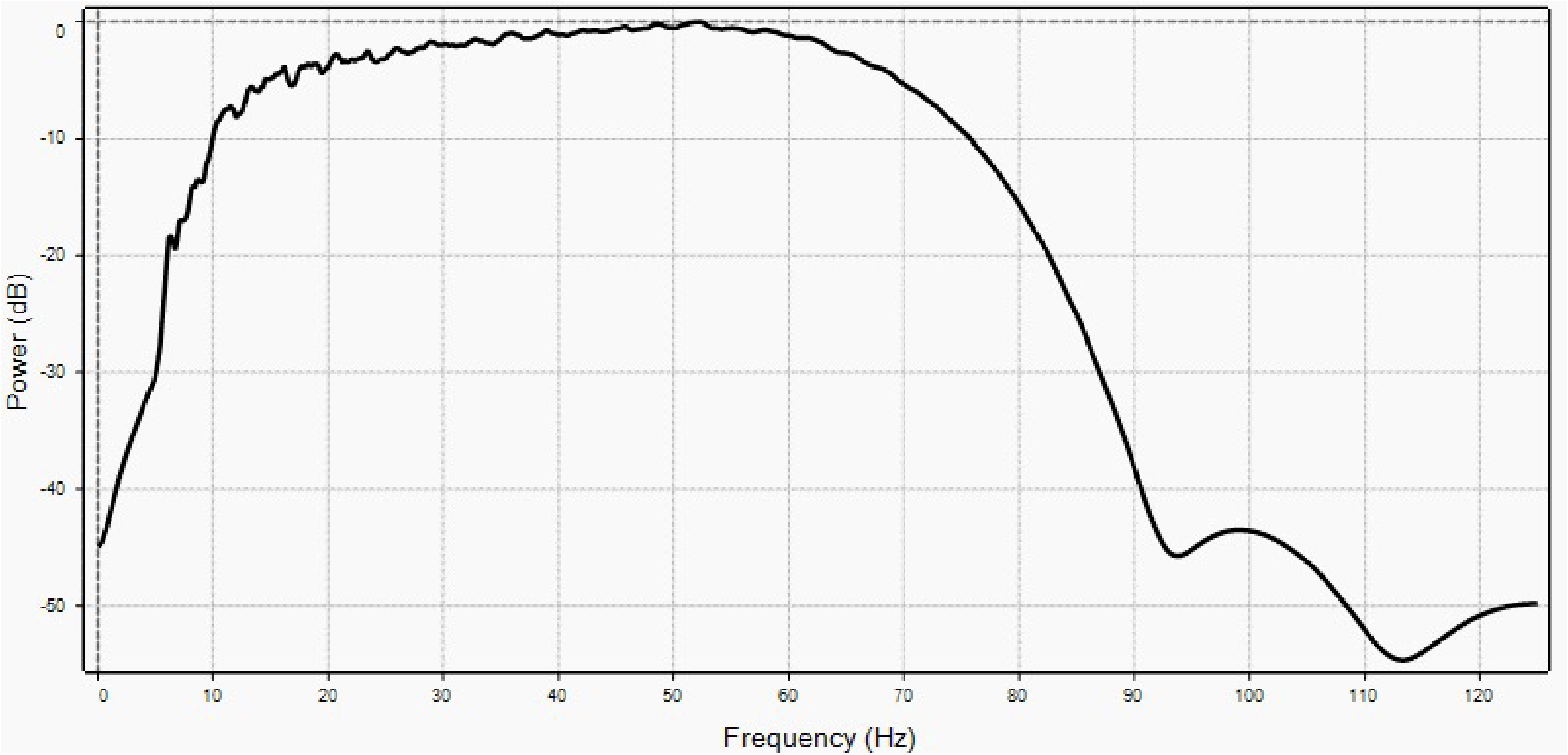

Frequency spectrum for the 3D seismic reflection dataset used in this study. The figure shows that the dominant frequency ranges between 40 – 60 Hz depending on the depth interval within the seismic survey.

Appendix 2 - detailed description of the methodology we use to calculate fault throw, displaccement, vertical slip and lateral propagation rates along with fault length/height aspect ratio

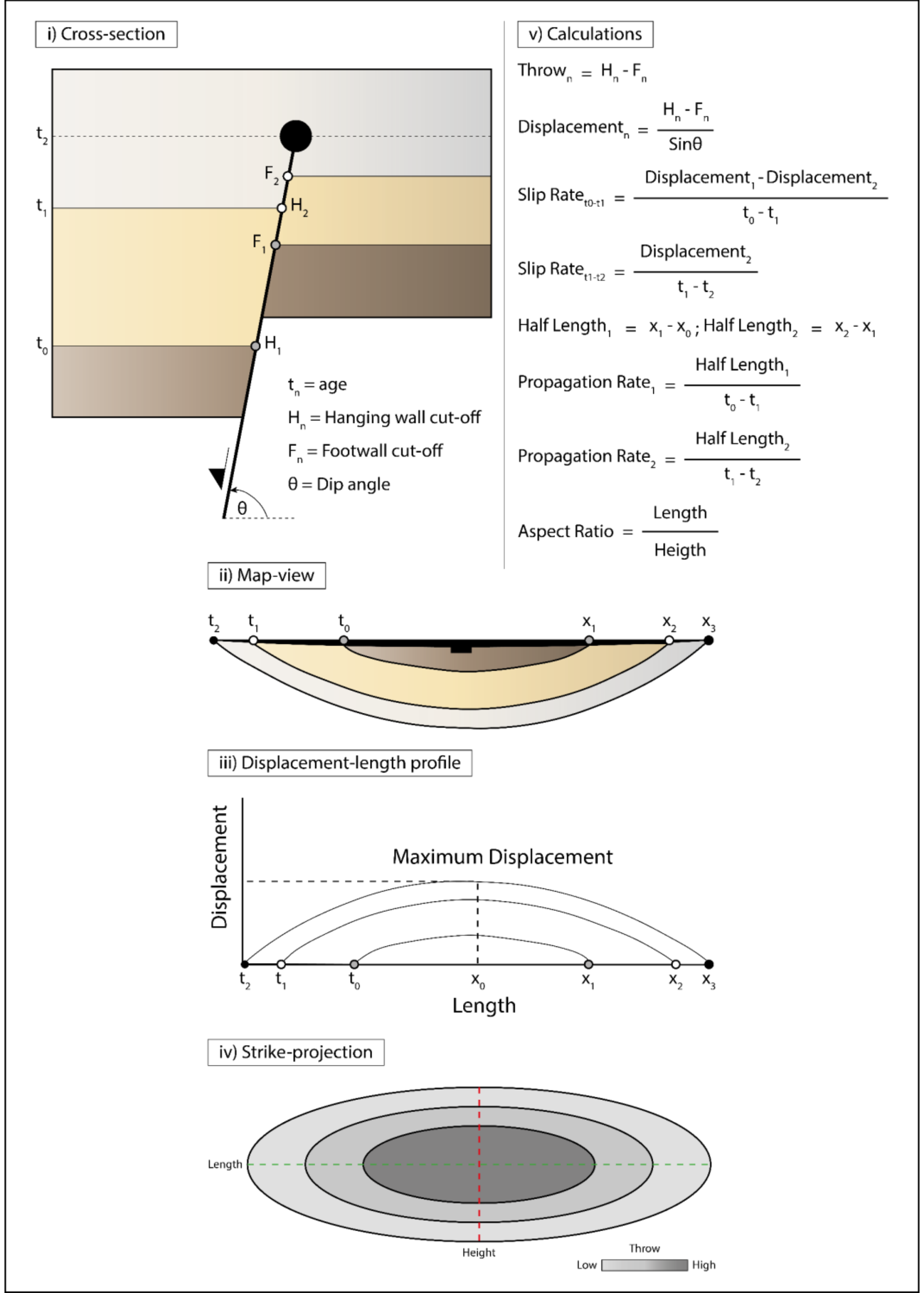

Appendix 3

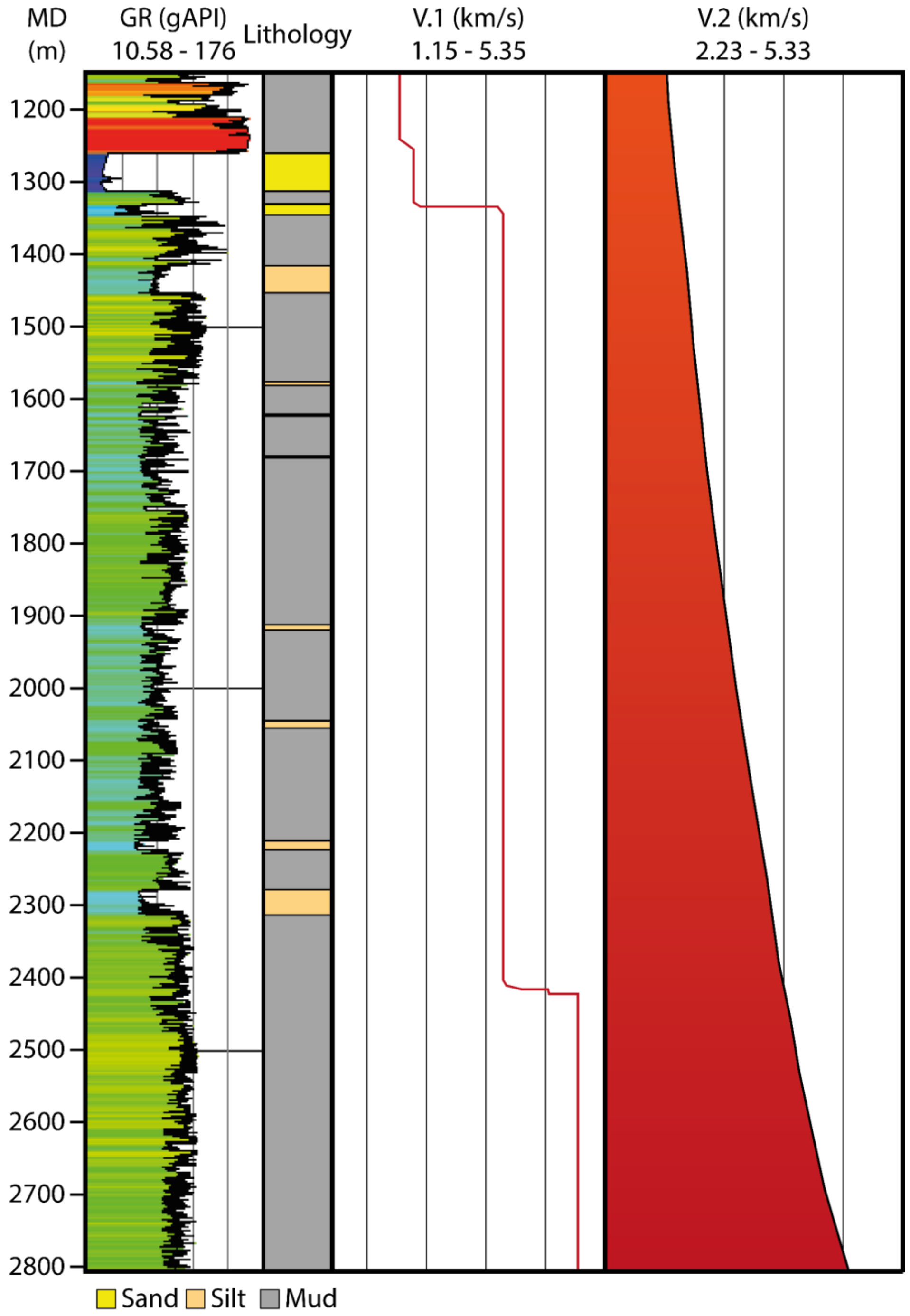

Well section view showing wireline and calculated logs for wellbore 7124/4-1S. The displayed data are for gamma ray (GR), interpreted lithology from GR, modelled interval velocity using simplified geological model (V.1), calculated pseudo interval velocity using estimated time - depth relationship from seismic well tie (V.2).

Appendix 4

A plot showing the compiled data from 29 different studies in addition to data from the current study. Detailed information about each study are provided in Appendix 6.

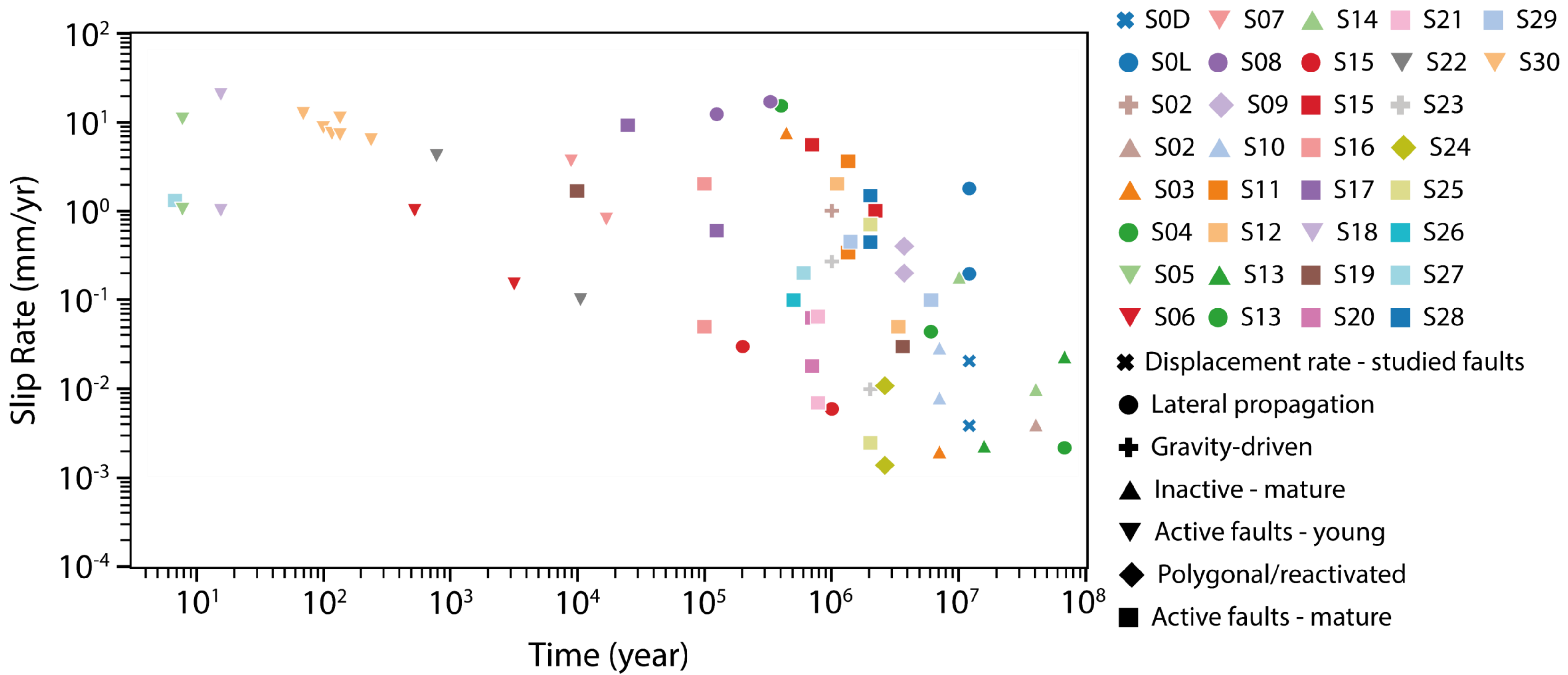

Appendix 5

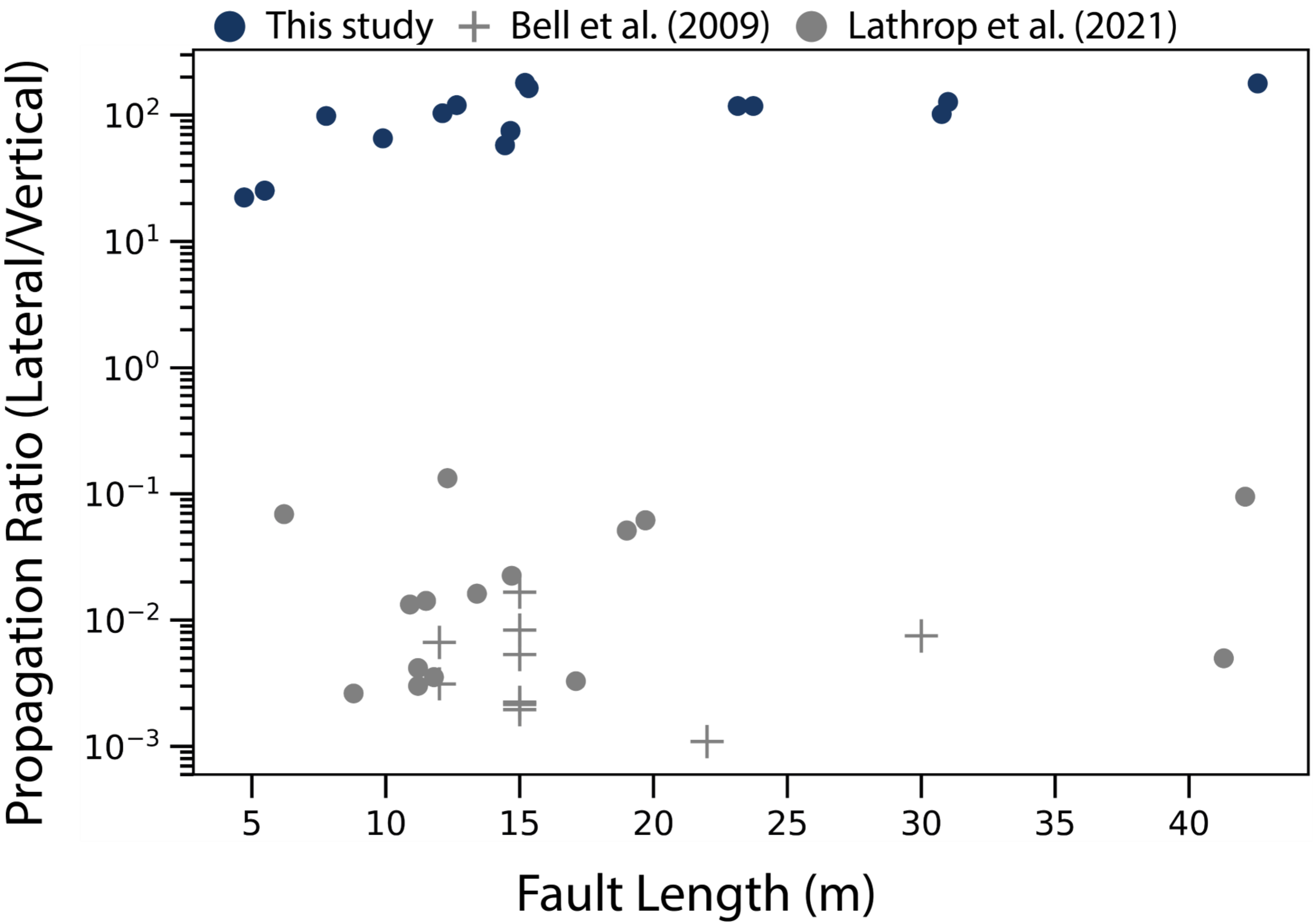
This study
Bell et al. (2009)
Lathrop et al. (2021)
Propagation Ratio (Lateral/Vertical)
10^{2}
10^{1}
10^{0}
10^{-1}
10^{-2}
10^{-3}
5
10
15
20
25
30
35
40
Fault Length (m)